Transport and Communications Science Journal, Vol. 77, Issue 09 (11/2026), 1226-1242

Transport and Communications Science Journal

ELECTRO-THERMOELASTIC VIBRATION OF FUNCTIONALLY GRADED POROUS SANDWICH PLATES WITH PIEZOELECTRIC AND STIFFENED LAYERS

Van-Tham Vu*

Faculty of Civil and Industrial Construction, Hanoi University of Civil Engineering (HUCE), 55 Giai Phong Road, Bach Mai Ward, Hanoi 100000, Vietnam

ARTICLE INFO

TYPE: Research Article
Received: 03/04/2026
Revised: 03/11/2026
Accepted: 10/11/2026
Published online: 15/11/2026
https://doi.org/10.47869/tcsj.77.9.8

* *Corresponding author*
Email: thamvv@huce.edu.vn

Abstract. A semi-analytical model is developed for the electro-thermoelastic free vibration of functionally graded porous sandwich plates with orthogonal stiffeners. The plate comprises a PoFGPie top face sheet, a porous metal-foam core, and a fully dense stiffened FGM bottom face sheet. A four-variable shear deformation theory (HSDT4), the Lekhnitskii smeared-stiffener model, and the pb²-Ritz method are combined in a unified formulation. A cosine-linear electric potential and uniform (UTR), linear (LTR), and nonlinear (NLTR) temperature rises are considered. The model is validated against published 3D, finite-element, and coupled-field solutions. Parametric studies cover core porosity, material gradation, layer thickness, stiffeners, voltage, geometry, boundary conditions, and thermal loading. Within the investigated ranges, increasing core porosity raises the fundamental dimensionless frequency because mass reduction dominates stiffness loss. Greater stiffener height raises the frequency, but the best stiffener orientation depends on the boundary condition and two-directional stiffening is not always optimal. Negative voltage produces a stiffening effect, positive voltage a softening effect, and thermal loading reduces the frequency, with UTR causing the largest decrease.

Keywords: electro-thermoelastic vibration, sandwich plate, porous material, piezoelectric material, HSDT4, pb²-Ritz method.

@ 2026 University of Transport and Communications

1. INTRODUCTION

Smart sandwich plates have attracted sustained interest because they combine load-carrying capability with sensing, control, and vibration tuning. Among smart materials, functionally graded piezoelectric (FGPie) media allow the electromechanical properties to vary continuously through the thickness, thereby alleviating the stress discontinuities typical of layered piezoelectric constructions. Introducing porosity into FGPie materials provides an additional means of tailoring stiffness, mass, and electromechanical coupling simultaneously, which is attractive for lightweight structures operating in multiphysics environments.

Various models have been developed for FGPie structures. Behjat et al. [1] used the finite element method together with first-order shear deformation theory to study the bending, vibration, and dynamic response of FGPie plates under mechanical, thermal, and electrical loads. Higher-order formulations were subsequently introduced to improve the description of through-thickness shear deformation, including the FGPie shell model of Wu et al. [2] and the three-dimensional elasticity solution of Sedighi and Shakeri [3]. Wang [4] investigated the electromechanical vibration of porous FGPie plates, while Zhong and Yu [5] derived an analytical solution for free and forced vibration. These studies show that material gradation and electric fields can markedly affect the dynamic characteristics of FGPie structures.

Porosity may arise during the fabrication of functionally graded materials and modifies the elastic, piezoelectric, and mass-density properties simultaneously. Barati and Zenkour [6] demonstrated pronounced combined effects of porosity, temperature, and electric field on the natural frequencies of FGPie plates. Studies of porous magneto-electro-elastic materials by Esen et al. [7] and Ebrahimi et al. [8] likewise showed that porosity patterns and coupled physical fields can substantially alter vibration behavior. Askari et al. [9, 10] investigated porous or porous-cellular plates coupled with piezoelectric effects and reported clear influences of porosity level, porosity distribution, and electrical conditions on the natural frequencies. More recently, Tran et al. [11] applied HSDT4 and the pb²-Ritz method to a piezoelectric functionally graded porous plate reinforced with graphene platelets. These studies clarify important material and electromechanical effects, but they do not include the orthogonal stiffener system adopted in the present configuration.

Besides tailoring the material architecture, stiffeners provide an efficient means of increasing plate stiffness with a relatively small mass penalty. For regularly spaced ribs, the Lekhnitskii smeared-stiffener approach [12-14] distributes the stiffener contributions into equivalent plate stiffnesses and therefore reduces the computational cost relative to modeling each stiffener explicitly. This approach is particularly convenient for parametric studies of stiffener number, dimensions, and orientation. In terms of plate kinematics, first-order shear deformation theory (FSDT) [15, 16] requires a shear-correction factor, whereas third-order shear deformation theory (TSDT) [17, 18] and higher-order theories describe the through-thickness shear strain more accurately. HSDT4 has been used effectively for stiffened smart sandwich structures by Pham et al. [19] and Vu and Tran [20], with the advantage of only four displacement variables and no shear-correction factor.

Although FGPie/PoFGPie plates, porous metal-foam structures, and stiffened plates have each been studied extensively, their combined treatment within a single electro-thermoelastic vibration model remains limited. In particular, the interaction among a voltage-driven PoFGPie top face sheet, a porous metal-foam core, and a fully dense FGM bottom face sheet reinforced by orthogonal stiffeners has not been systematically examined together with different boundary

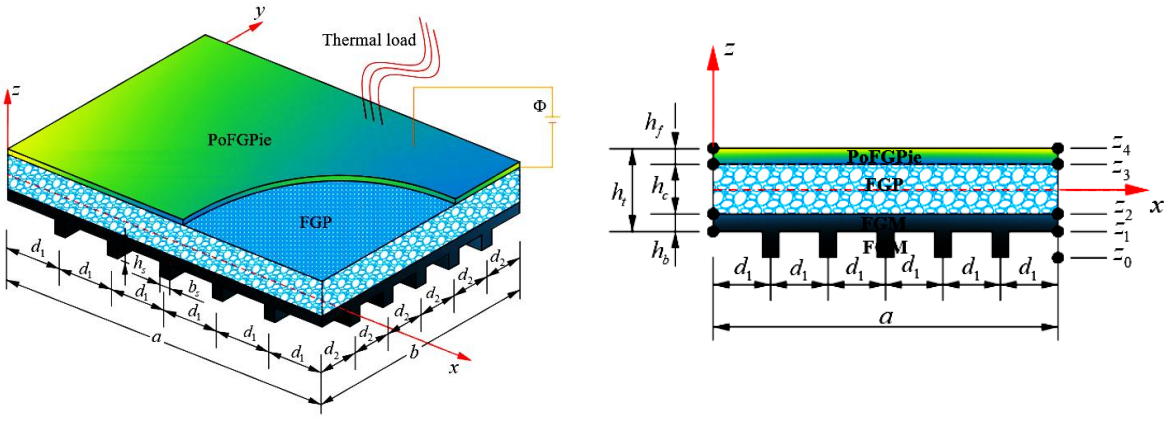
conditions. The combined effects of stiffener number and size, material-gradation indices, layer-thickness configuration, applied voltage, and temperature profile on the vibration frequency also remain insufficiently documented. This is the gap addressed in the present study. The structural configuration and coupling scope therefore extend the unstiffened systems in [9-11] and differ from the stiffened smart-sandwich models in [19, 20], which employ other core and smart-face configurations.

Accordingly, this study develops a semi-analytical model for the electro-thermoelastic free vibration of an SFGP–Pie sandwich plate composed of a PoFGPie top face sheet, a porous metal-foam core, and a fully dense FGM bottom face sheet reinforced by orthogonal stiffeners. The displacement field is described by HSDT4, the stiffeners are represented by the Lekhnitskii smeared model, and the solution is constructed using the pb²-Ritz method to accommodate several boundary conditions within a unified framework. The electric potential in the PoFGPie layer is represented by a cosine-linear distribution, and three temperature fields—uniform thermal rise (UTR), linear thermal rise (LTR), and nonlinear thermal rise (NLTR)—are considered. After validation against published results, the model is used to examine the effects of core porosity, material-gradation indices, layer-thickness ratio, stiffener number and size, applied voltage, plate geometry, boundary conditions, and thermal loading on the fundamental frequency. The smeared-stiffener model is intended for uniformly distributed ribs and global response; local stiffener effects, interface slip, and delamination are outside the scope.

2. THEORETICAL FORMULATION

2.1. Plate configuration and material description

Consider a rectangular sandwich plate of dimensions $a \times b \times h$. The xy plane coincides with the plate mid-plane and the z-axis is normal to the plate. Through the thickness, the structure comprises a fully dense FGM bottom face sheet, a porous metal-foam core, and a PoFGPie top face sheet with thicknesses h_b, h_c, and h_f, respectively, where $h = h_b + h_c + h_f$. The layer interfaces are located at $z_1 = -h/2$, $z_2 = z_1 + h_b$, $z_3 = z_2 + h_c$, and $z_4 = h/2$. Two orthogonal families of FGM stiffeners are attached to the lower surface. For a stiffener family oriented along α $(\alpha = x, y)$, the width, height, smeared spacing, and lower coordinate are $b_{s\alpha}$, $h_{s\alpha}$, d_α, and $z_{0\alpha} = z_1 - h_{s\alpha}$, respectively. Perfect bonding is assumed between adjacent layers and between the stiffeners and the bottom face sheet. The geometry is shown in Fig. 1.



(a) (b)

Figure 1. Geometry of the orthogonally stiffened SFGP–Pie sandwich plate:
(a) three-dimensional view; (b) cross-section.

The PoFGPie face sheet is modeled as a two-phase PZT-4/$BaTiO_3$ material. For a generic material property $\Xi \in \{c_{ij}, e_{ij}, \kappa_{ij}, \alpha_i, \rho\}$, the porous gradation law is written as [21, 22].

For convenience, define $P_\Xi(z) = e_0^{Pie}/2\left(\Xi_u^{Pie} + \Xi_l^{Pie}\right)\varphi^{Pie}(z)$ as the porosity-induced reduction term. Then

$$\Xi^{Pie}(z) = \Xi_l^{Pie} + \left(\Xi_u^{Pie} - \Xi_l^{Pie}\right)V_{BaTiO_3}(z) - P_\Xi(z). \tag{1}$$

where Ξ^{Piel} and Ξ^{Pieu} denote the corresponding properties of PZT-4 and $BaTiO_3$, respectively, and ${e_0}^{\mathrm{Pie}}$ is the porosity coefficient. The $BaTiO_3$ volume fraction V_{BaTiO_3} is defined by

$$V_{BaTiO_3}(z) = \left(\frac{z - z_4}{z_3 - z_4}\right)^{p_{Pie}}, \qquad z_3 \le z \le z_4, \tag{2}$$

where p_{Pie} is the material-gradation index. Two porosity patterns are considered for the PoFGPie face sheet:

$$\varphi^{Pie}(z) = \begin{cases} 1, & \text{FGPie-I,} \\ 1 - 2|z|/h, & \text{FGPie-II.} \end{cases} \tag{3}$$

The properties of the two piezoelectric constituents are listed in Table 1; the thermal-expansion coefficients are included for consistency with the thermal analysis.

Table 1. Material properties of $BaTiO_3$ and PZT-4.

Phase	c_{11}	c_{12}	c_{13}	c_{33}	c_{55}	e_{31}	e_{33}	e_{15}	κ_{11}	κ_{33}	ρ	α
$BaTiO_3$ [23]	166	77	78	162	43.0	−4.4	18.6	11.6	11.2	12.6	5800	15.8
PZT-4 [23]	139	77.8	74	115	25.6	−5.2	15.1	12.7	6.46	5.62	7500	2.0

Notes: *cij* in GPa; *eij* in C/m^2; *κij* in 10^{-9} C^2/(N·m^2); ρ in kg/m^3; and α in 10^{-6} K^{-1}.

For the porous metal-foam core, Young's modulus and mass density are described by

$$E^c(z) = E_0[1 - e_0\lambda(z)], \qquad \rho^c(z) = \rho_0[1 - e_m\lambda(z)] \tag{4}$$

where $e_m = 1 - \sqrt{1 - e_0}$, $E_0 = 200$ GPa, $\rho_0 = 7850$ kg/m^3, $\nu_c = 1/3$, and $\alpha_c = 23 \times 10^{-6}$ K^{-1}. According to the distribution functions adopted in the model, the two core-porosity patterns are termed the symmetric porosity distribution (SPD) and asymmetric porosity distribution (ASPD):

$$\lambda(z) = \begin{cases} \cos(\pi z/h_c), & \text{SPD,} \\ \cos(\pi z/(2h_c) + \pi/4), & \text{ASPD.} \end{cases} \tag{5}$$

The bottom face sheet and stiffeners are fully dense Al/Al_2O_3 FGM. With $r = b$ for the bottom face sheet and $r = s\alpha$ for the stiffeners oriented along α, a generic material property is evaluated by the rule of mixtures

$$\Xi^{(r)}(z) = \Xi_m + (\Xi_c - \Xi_m)V_c^{(r)}(z), \tag{6}$$

where

$$V_c^{(b)}(z) = \left(\frac{z - z_2}{z_1 - z_2}\right)^{p_z}, \qquad V_c^{(s\alpha)}(z) = \left(\frac{z_{0\alpha} - z}{z_{0\alpha} - z_1}\right)^{p_z}. \tag{7}$$

Here p_z is the FGM gradation index. The Al_2O_3/Al constituents have $E_c = 380$ GPa, $E_m = 70$ GPa, $\rho_c = 3800$ kg/m^3, $\rho_m = 2707$ kg/m^3, $\nu = 0.3$, $\alpha_c = 7 \times 10^{-6}$ K^{-1}, and $\alpha_m = 23 \times 10^{-6}$ K^{-1}.

2.2. HSDT4 kinematics and coupled fields

According to HSDT4 [24-26], the displacement field is assumed as

$$u = u_0 - z\,w_{b,x} - f(z)w_{s,x}, \quad v = v_0 - z\,w_{b,y} - f(z)w_{s,y}, \quad w = w_b + w_s. \tag{8}$$

where u_0 and v_0 are the in-plane displacements of the mid-plane, while w_b and w_s are the transverse displacement components associated with bending and shear, respectively. The following thickness function is used consistently in the numerical implementation:

$$f(z) = z\left[-\frac{3}{8} + \frac{11}{6}\left(\frac{z}{h}\right)^2\right], \qquad g(z) = 1 - f'(z). \tag{9}$$

With this choice, $g(\pm h/2) = 0$, so the transverse shear stresses vanish at the outer surfaces without a shear-correction factor. The in-plane and transverse-shear strain vectors can be written compactly as

$$\boldsymbol{\varepsilon}_p = \boldsymbol{\varepsilon}_0 + z\boldsymbol{\kappa}_b + f(z)\boldsymbol{\kappa}_s, \qquad \boldsymbol{\gamma}_s = g(z)\begin{Bmatrix} w_{s,x} \\ w_{s,y} \end{Bmatrix}, \tag{10}$$

where

$$\boldsymbol{\varepsilon}_0 = \begin{Bmatrix} u_{0,x} \\ v_{0,y} \\ u_{0,y} + v_{0,x} \end{Bmatrix}, \qquad \boldsymbol{\kappa}_b = -\begin{Bmatrix} w_{b,xx} \\ w_{b,yy} \\ 2w_{b,xy} \end{Bmatrix}, \qquad \boldsymbol{\kappa}_s = -\begin{Bmatrix} w_{s,xx} \\ w_{s,yy} \\ 2w_{s,xy} \end{Bmatrix}. \tag{11}$$

For the core, bottom FGM face sheet, and stiffeners, the constitutive relation is written as $\boldsymbol{\sigma} = \mathbf{Q}(z)(\boldsymbol{\varepsilon} - \boldsymbol{\varepsilon}^T)$, where $\boldsymbol{\varepsilon}^T = \{\alpha_x \Delta T, \alpha_y \Delta T, 0,0,0\}^T$ is the thermal-strain vector. For the PoFGPie layer, the electromechanically coupled constitutive equations are used under the plane-stress condition through the thickness:

$$\boldsymbol{\sigma}^{Pie} = \overline{\mathbf{C}}(\boldsymbol{\varepsilon} - \boldsymbol{\varepsilon}^T) - \overline{\mathbf{e}}^T\mathbf{E}, \qquad \mathbf{D} = \overline{\mathbf{e}}\boldsymbol{\varepsilon} + \overline{\boldsymbol{\kappa}}\mathbf{E}, \tag{12}$$

where $\mathbf{E} = -\nabla\Phi$ and $\mathbf{D}$ are the electric field and electric-displacement vector, respectively. The principal reduced coefficients are obtained from

$$\overline{C}_{11} = C_{11} - \frac{C_{13}^2}{C_{33}}, \qquad \overline{C}_{12} = C_{12} - \frac{C_{13}^2}{C_{33}}, \qquad \overline{e}_{31} = e_{31} - \frac{C_{13}e_{33}}{C_{33}} \tag{13}$$

In addition, $\overline{\kappa}_{33} = \kappa_{33} + e_{33}^2/C_{33}$, $\overline{C}_{22} = \overline{C}_{11}$, $\overline{C}_{44} = \overline{C}_{55} = C_{55}$, $\overline{C}_{66} = \left(\overline{C}_{11} - \overline{C}_{12}\right)/2$, $\overline{e}_{15} = e_{15}$, and $\overline{\kappa}_{11} = \kappa_{11}$.

The electric potential in the PoFGPie layer is represented by the cosine-linear distribution of Wang [27], written using the same thickness coordinate as in the numerical implementation:

$$\Phi(x,y,z,t) = -\phi_0(x,y,t)\cos\vartheta + \frac{2V}{\pi}\vartheta, \qquad \vartheta = \frac{\pi(z - z_m)}{h_f}, \qquad z_m = (z_3 + z_4)/2, \qquad z_3 \le z \le z_4, \tag{14}$$

where V is the applied voltage and $\phi_0(x,y,t)$ is the unknown two-dimensional electric potential. The linear term represents the prescribed voltage, whereas the trigonometric term accounts for the unknown coupled potential. Under the quasi-static assumption, the electric field is obtained from the electric-potential gradient. The electrical boundary condition is prescribed voltage, corresponding to actuation; open-circuit and sensing conditions are not considered. The sensitivity of the results to alternative through-thickness potential functions is not examined here; therefore, the reported results are understood within the adopted cosine-linear assumption.

$$E_x = \phi_{0,x}\cos\vartheta, \qquad E_y = \phi_{0,y}\cos\vartheta, \qquad E_z = -\frac{\pi}{h_f}\phi_0\sin\vartheta - \frac{2V}{h_f}. \tag{15}$$

The material coefficients are assumed to be temperature-independent over the investigated range. For each material segment k bounded by z_k^L and z_k^U, introduce the local coordinate $\eta_k = (z - z_k^L)/(z_k^U - z_k^L)$. The following three temperature-rise profiles are applied consistently to each layer and to the stiffeners:

$$\Delta T_k(z) = \begin{cases} \Delta T, & \text{UTR,} \\ \Delta T\,\eta_k, & \text{LTR,} \\ \Delta T\left[1 - \cos\left(\frac{\pi}{2}\eta_k\right)\right], & \text{NLTR.} \end{cases} \tag{16}$$

This local-coordinate definition allows the same temperature law to be applied consistently to the bottom FGM face sheet, the core, the PoFGPie face sheet, and the portions of the stiffeners located outside the plate thickness.

2.3. Thickness-integrated quantities and pb²-Ritz solution

After substituting the kinematic and constitutive relations into Hamilton's principle, the contributions of the three layers and stiffeners are integrated through the thickness. Using the generic notation R_j for the membrane, membrane–bending coupling, bending, higher-order, and transverse-shear stiffness resultants, one may write

$$R_j = R_j^{pl} + R_j^{st}, \qquad R_j^{pl} = \sum_{k=1}^{3}\int_{z_k^L}^{z_k^U} Q_j^{(k)}(z)\,\psi_j(z)\,dz \tag{17}$$

and, according to the Lekhnitskii smeared-stiffener model [12-14],

$$R_j^{st} = \sum_{\alpha=x,y}\frac{b_{s\alpha}}{d_\alpha}\int_{z_{0\alpha}}^{z_1} Q_j^{(s\alpha)}(z)\,\psi_j(z)\,dz, \tag{18}$$

where $\psi_j(z)$ takes the forms 1, z, z^2, $f(z)$, $zf(z)$, $f^2(z)$, or $g^2(z)$, depending on the resultant considered. The smeared representation is intended for the global response of uniformly distributed stiffeners; local stresses at the stiffener roots and local stiffener modes are outside the scope of the model.

The thermal field and applied voltage generate initial in-plane resultants. In the vibration analysis, these resultants are retained in the geometric-stiffness matrix through

$$N_x^0 = N_x^T + N_x^E, \qquad N_y^0 = N_y^T + N_y^E, \tag{19}$$

where N^T and N^E are obtained by through-thickness integration of the thermal and electrically induced stresses, respectively. The eigenvalue problem is therefore formulated about a thermally and electrically pre-stressed state rather than neglecting these membrane resultants.

For the inertia terms, the mass of each stiffener family is converted into an equivalent distributed mass within the bottom FGM face sheet. Define

$$m_{s\alpha} = \int_{z_{0\alpha}}^{z_1}\rho_{s\alpha}(z)\,dz, \qquad \rho_b^{eq}(z) = \rho_b(z) + \frac{1}{h_b}\sum_{\alpha=x,y}\frac{b_{s\alpha}}{d_\alpha}m_{s\alpha}. \tag{20}$$

The system inertia moments are then evaluated consistently using the equivalent density:

$$\left(I_0, I_1, I_2, I_f, I_{zf}, I_{f^2}\right) = \sum_{k=1}^{3} \int_{z_k^L}^{z_k^U} \rho_k\,(z)\,\Theta(z)\,dz \tag{21}$$

where $\Theta(z) = (1, z, z^2, f, zf, f^2)$, and $\rho_b(z)$ in the bottom face sheet is replaced by $\rho_b^{eq}(z)$. This representation preserves the smeared stiffener mass and is consistent with the implementation used in the validation cases.

In the pb²-Ritz method [28], each generalized field $\chi \in \{u_0, v_0, w_b, w_s, \phi_0\}$ is approximated over the normalized domain $-1 \le \xi, \eta \le 1$ as

$$\chi(\xi,\eta) = B_\chi(\xi,\eta) \sum_{q=0}^{M_R} \sum_{s=0}^{q} d_{qs}^{(\chi)}\, \xi^{q-s} \eta^s, \qquad \xi = \frac{2x}{a} - 1, \quad \eta = \frac{2y}{b} - 1. \tag{22}$$

The boundary functions are written as

$$B_u = B_v = \prod_{i=1}^{4} L_i^{r_i}, \qquad B_w = B_\phi = \prod_{i=1}^{4} L_i^{s_i}, \tag{23}$$

where $L_1 = \eta + 1, L_2 = \xi - 1, L_3 = \eta - 1, L_4 = \xi + 1$. For each edge i, the exponent pair r_i, s_i is selected as (1,2) for a clamped edge C, (0,1) for a simply supported edge S, and (0,0) for a free edge F. Accordingly, $B_u = B_v$ imposes the essential conditions for the in-plane displacements, whereas $B_w = B_\phi$ is used for the transverse displacement variables and the electric-potential variable. The symbols C, S, and F denote clamped, simply supported, and free edges, respectively; SSSS, CCCC, SCSC, and SCSF follow the four-edge order used throughout the paper.

After substituting the Ritz approximations into the functional and applying the stationarity condition, the coupled electromechanical algebraic system is written as

$$\begin{bmatrix} \mathbf{K}_{mm} + \mathbf{K}_G & \mathbf{K}_{m\phi} \\ \mathbf{K}_{\phi m} & \mathbf{K}_{\phi\phi} \end{bmatrix} \begin{Bmatrix} \mathbf{d}_m \\ \mathbf{d}_\phi \end{Bmatrix} - \omega^2 \begin{bmatrix} \mathbf{M} & \mathbf{0} \\ \mathbf{0} & \mathbf{0} \end{bmatrix} \begin{Bmatrix} \mathbf{d}_m \\ \mathbf{d}_\phi \end{Bmatrix} = \mathbf{0}, \tag{24}$$

where K_{mm} is the mechanical stiffness matrix; K_G is the geometric-stiffness matrix generated by the initial in-plane resultants ${N_x}^0, {N_y}^0$, including both thermal and electrical contributions; $K_{m\phi}, K_{\phi m}$ are the electromechanical coupling matrices; $K_{\phi\phi}$ is the dielectric matrix; and M is the mechanical mass matrix. Under the quasi-static electric-field assumption, the electrical degrees of freedom carry no inertia. Static condensation of the electrical variables from the second row of Eq. (24) gives the equivalent mechanical eigenvalue problem

$$\mathbf{K}_{eff} = \mathbf{K}_{mm} + \mathbf{K}_G - \mathbf{K}_{m\phi}\mathbf{K}_{\phi\phi}^{-1}\mathbf{K}_{\phi m}, \qquad \left(\mathbf{K}_{eff} - \omega^2\mathbf{M}\right)\mathbf{d}_m = \mathbf{0}. \tag{25}$$

In the eigenvalue problem, the quantity obtained directly is $\lambda = \omega^2$. Only positive eigenvalues $\lambda > 0$ correspond to stable vibration; $\lambda = 0$ marks the onset of instability, whereas $\lambda < 0$ represents an unstable state and does not yield a real natural frequency. As the fundamental eigenvalue approaches zero from the positive side, the system approaches prestress-induced instability. The dimensionless frequency used below is defined by $\overline{\omega} = (\omega a^2/h)\sqrt{(p_{BaTiO3}/c_{11}^{BaTiO3})}$.

3. RESULTS AND DISCUSSION

3.1. Validation and convergence

Before the parametric studies, convergence and accuracy are assessed using three independent benchmark groups. First, Table 2 compares the first four dimensionless frequencies of a fully clamped FGM sandwich plate with the three-dimensional solution of Li et al. [29]. As the Ritz polynomial order p_r increases from 2 to 7, the frequencies converge steadily. At p_r=7, the absolute differences of the first four modes from the 3D solution are approximately 0.17%, 0.63%, 0.63%, and 1.27%, respectively. Therefore, p_r=8 is used in the subsequent calculations.

Table 2. Convergence and comparison of the first four dimensionless frequencies of a CCCC FGM sandwich plate.

Method	p_r	$\overline{\omega}_1$	$\overline{\omega}_2$	$\overline{\omega}_3$	$\overline{\omega}_4$
Present	2	2.29370	4.57245	4.57245	6.49445
Present	4	2.28869	4.51706	4.51706	6.46693
Present	5	2.28651	4.50595	4.50595	6.46693
Present	6	2.28651	4.49541	4.49541	6.44980
Present	7	2.28651	4.49541	4.49541	6.43099
3D [29]	-	2.29049	4.46721	4.46721	6.35053
Difference from 3D [29] (%)		0.174	0.631	0.631	1.267

The applicability of the smeared-stiffener model is examined separately using the fully clamped isotropic plate with orthogonal stiffeners studied by Harik and Guo [30]. The benchmark contains five stiffeners in one direction and three in the orthogonal direction, and therefore represents a relatively low stiffener count. As shown in Table 3, the differences in the first three frequencies relative to the finite element method (FEM) results [30] are only 0.452%, 0.382%, and 1.993%; the pb²-Ritz–TSDT results in [18] lie in the same range. The agreement indicates that the smeared model is sufficiently accurate for the global vibration response of the uniformly distributed stiffeners considered here. It is not intended, however, to resolve local stresses at stiffener roots or local modes of individual stiffeners.

Table 3. Comparison of the natural frequencies f (Hz) of a CCCC plate with orthogonal stiffeners.

Mode	pb²-Ritz TSDT [18]	FEM [30]	Present	Difference from FEM (%)
1	812.800	822.300	826.018	0.452
2	1215.600	1234.900	1239.613	0.382
3	1956.100	1994.100	2033.839	1.993

The electromechanical coupling and through-thickness electric-potential interpolation are further checked against the functionally graded magneto-electro-elastic (MEE-FG) plate of Ebrahimi et al. [8] with zero externally applied magnetic potential. The MEE coupling coefficients of the reference material are retained in this comparison; thus, the benchmark is not reduced to a purely piezoelectric material. Table 4 shows a maximum absolute difference of only 0.018%, supporting the coupled electromechanical integration and the cosine-linear potential representation used in the present model.

Table 4. Validation of the dimensionless frequency against the MEE-FG plate results in [8].

p	FGPie-I [8]	Present	Difference (%)	FGPie-II [8]	Present	Difference (%)
0.2	4.43465	4.43400	-0.015	4.53203	4.53121	-0.018
1	4.19929	4.19875	-0.013	4.32975	4.32902	-0.017
5	4.02586	4.02532	-0.013	4.17839	4.17774	-0.016

The three benchmark groups assess, respectively, Ritz-basis convergence, the smeared-stiffener representation, and the coupled electromechanical branch. The small quantitative differences in all three cases support the use of the model in the following parametric studies.

3.2. Parametric studies

Unless otherwise stated, the calculations use a=b=1 m, a/h=50, the layer-thickness configuration 1-8-1, an FGPie-I PoFGPie face with e_0^{Pie}=0.2 and p_{Pie}=p_z=1, an SPD porous core with e_0^c=0.6, n_x=n_y=5, b_s=1.5h, h_s=2h, V=0, and ΔT=0. The core distributions SPD and ASPD refer to the functions defined in Section 2.1.

3.2.1. Effects of core porosity and material-gradation indices

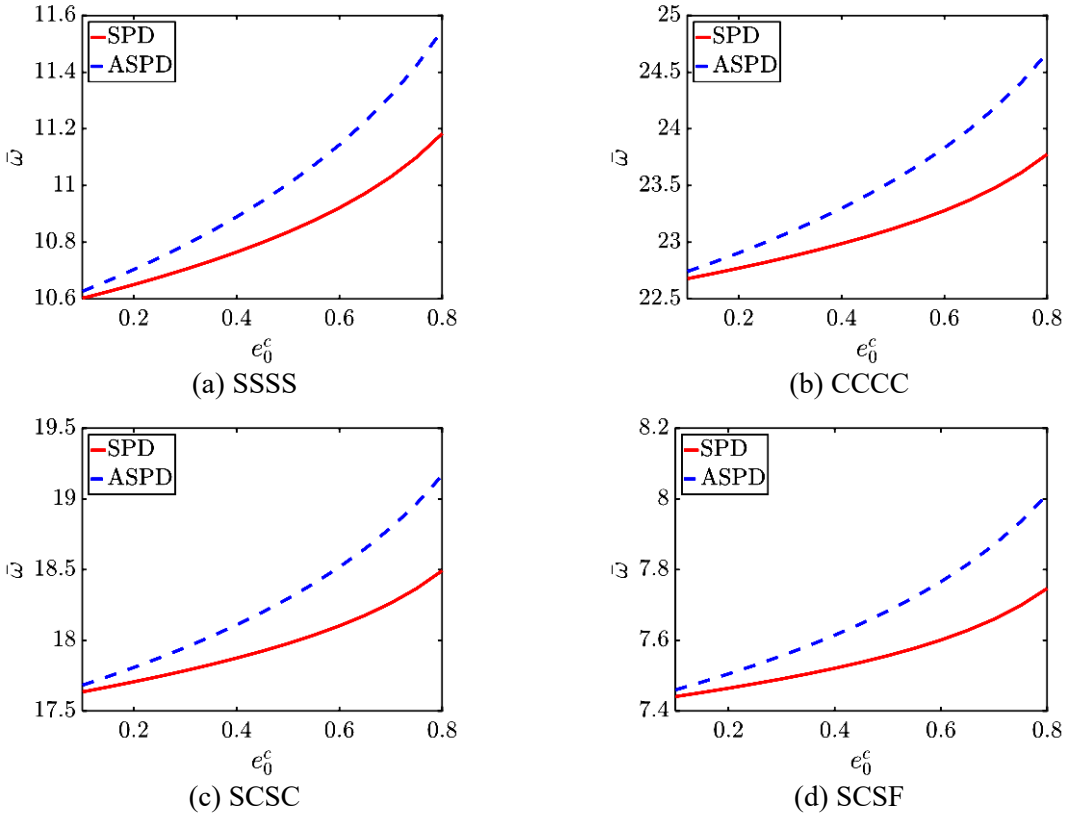
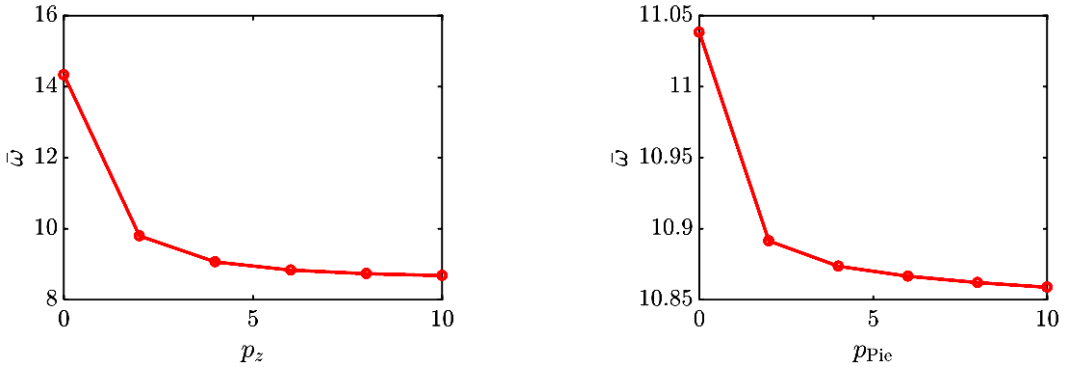


Figure 2. Effect of the core porosity coefficient and porosity distribution on the dimensionless frequency.

Figure 2 shows the effect of the core porosity coefficient e_0. For all four boundary conditions, $\overline{\omega}$ increases with e_0 over the investigated range. This behavior results from two competing effects: porosity reduces both equivalent stiffness and mass, but for the present material model and configuration, the mass reduction dominates the stiffness loss in the

stiffness-to-mass ratio governing the frequency. ASPD gives slightly higher values than SPD, and the difference increases with porosity. The frequency ordering remains CCCC > SCSC > SSSS > SCSF, consistent with the increasing degree of boundary restraint.

Figure 3 shows that the two material-gradation indices have markedly different effects. As p_z increases from 0 to 10, the SSSS frequency decreases from 14.3297 to 8.6811, a reduction of about 39.4%. Over the same range of p_{Pie}, the frequency changes only from 11.0383 to 10.8588, or about 1.63%. Because p_z controls both the bottom FGM face sheet and the stiffeners, whereas the PoFGPie face is relatively thin, the response is much more sensitive to p_z than to p_{Pie}.



(a) p_z (b) p_{Pie}

Figure 3. Effect of (a) the p_z index and (b) the p_{Pie} index on $\overline{\omega}$ of the SSSS plate.

3.2.2. Effects of layer-thickness ratio and stiffeners

Table 5 presents the influence of layer-thickness configuration for the 1-1-1, 1-4-1, and 1-8-1 cases. For the SPD core, the frequency decreases slightly as the core fraction increases for all four boundary conditions. For the ASPD core, the changes are much smaller and are not strictly monotonic; in some cases, the frequency decreases slightly and then rises again. The effect of layer-thickness ratio therefore cannot be reduced to a single monotonically decreasing trend for all porosity distributions. Instead, it reflects the competition among changes in core mass, core stiffness, and the contributions of the two face sheets.

Table 5. Effect of layer-thickness configuration on the dimensionless frequency.

BC	Core distribution	1-1-1	1-4-1	1-8-1
SSSS	SPD	11.1253	10.9503	10.9215
	ASPD	11.1918	11.1391	11.1440
CCCC	SPD	23.6692	23.3256	23.2790
	ASPD	23.8077	23.7612	23.8318
SCSC	SPD	18.4198	18.1435	18.1030
	ASPD	18.5276	18.4757	18.5188
SCSF	SPD	7.7321	7.6167	7.6012
	ASPD	7.7780	7.7524	7.7661

For Table 6 and Fig. 4, an ASPD core with a porosity coefficient of 0.2 is considered. The effects of stiffener number and orientation are summarized in Table 6 and Fig. 4. Three arrangements are considered: stiffeners only along x, only along y, and in both directions. For SSSS and CCCC, the two one-directional cases coincide because of the symmetry of the square

plate and its boundary conditions. As the number of stiffeners increases from 0 to 9, the frequency increases for every arrangement, including SCSF. For SCSC and SCSF, the increase depends strongly on stiffener orientation because of the asymmetric restraint. For example, for SCSF, stiffeners along x raise the frequency by about 20.8% as n increases from 0 to 9, whereas stiffeners along y and in both directions produce increases of about 135.6% and 126.8%, respectively. For $n \geq 5$, the y-only arrangement gives a slightly higher frequency than the two-directional arrangement. Thus, stiffening efficiency depends on the interaction between rib orientation and asymmetric boundary restraint, and two-directional stiffening does not necessarily produce the largest frequency when a free edge is present.

Table 6. Effect of stiffener number and orientation on the dimensionless frequency.

BC	Arrangement	0	3	5	7	9
SSSS	x	5.6269	8.0314	8.6068	9.0016	9.2812
	y	5.6269	8.0314	8.6068	9.0016	9.2812
	$x+y$	5.6269	9.8155	10.7037	11.2875	11.6837
CCCC	x	10.2308	16.8020	18.3382	19.4045	20.1719
	y	10.2308	16.8020	18.3382	19.4045	20.1719
	$x+y$	10.2308	20.8714	22.9064	24.2030	25.0569
SCSC	x	8.2415	15.6940	17.3238	18.4424	19.2434
	y	8.2415	9.9355	10.3816	10.6922	10.9110
	$x+y$	8.2415	16.2595	17.8086	18.7986	19.4533
SCSF	x	3.5814	4.0793	4.1955	4.2736	4.3263
	y	3.5814	6.8846	7.5996	8.0883	8.4373
	$x+y$	3.5814	6.9032	7.5053	7.8800	8.1219

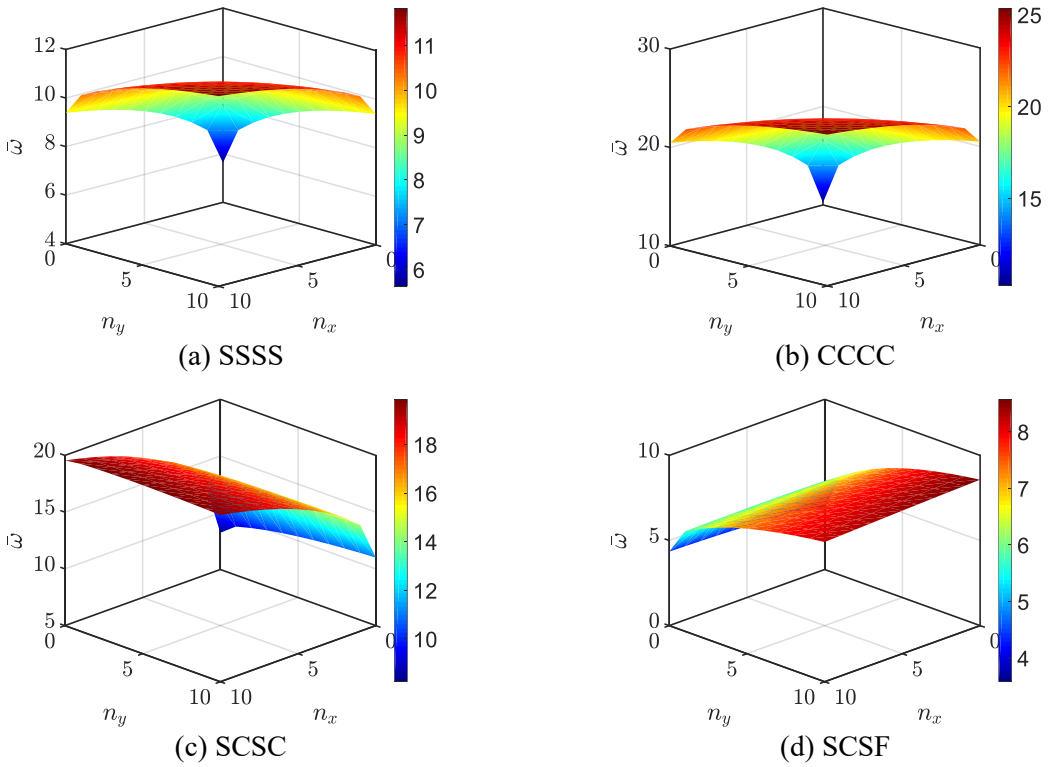
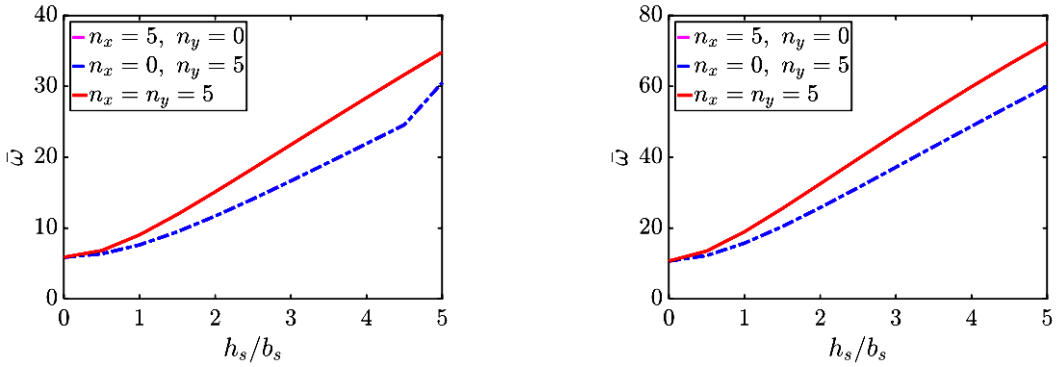


Figure 4. Effect of stiffener number and orientation on the dimensionless frequency.

Figure 5 examines the stiffener cross-sectional ratio h_s/b_s. With b_s fixed, increasing h_s clearly raises the frequency because both the sectional moment of inertia and the bending stiffness of the stiffener system increase. For the square SSSS and CCCC plates, the curves for stiffeners only along x and only along y coincide by symmetry; two-directional stiffening gives the highest frequency for these two symmetric boundary conditions.



(a) SSSS (b) CCCC

Figure 5. Effect of h_s/b_s on the dimensionless frequency: (a) SSSS; (b) CCCC.

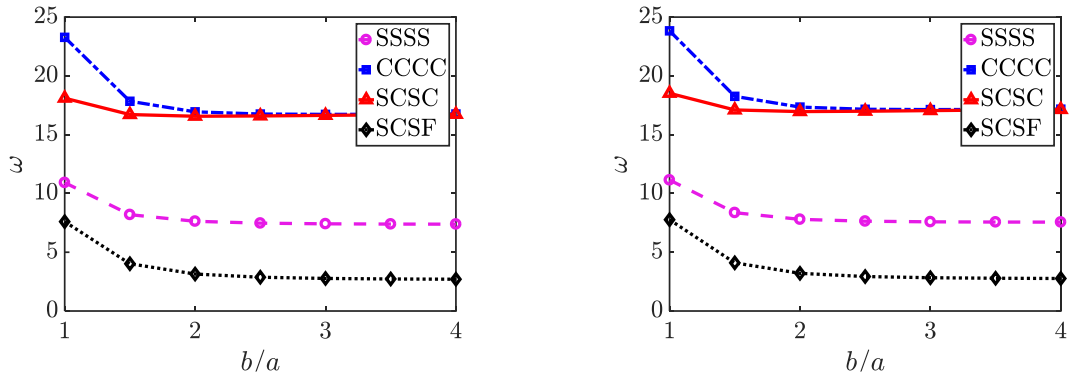
3.2.3. Effects of applied voltage and plate geometry

Table 7 presents the effect of applied voltage for three face-sheet states: FGPie-0 (nonporous), FGPie-I, and FGPie-II. For every boundary condition and all three face states, the frequency decreases as V increases from -1200 V to +1200 V. Under the sign convention adopted here, negative voltage generates an electrically induced membrane force with a stiffening effect, whereas positive voltage produces a softening effect; these membrane forces are retained in the geometric stiffness of the eigenvalue problem. The differences among FGPie-0, FGPie-I, and FGPie-II are small and do not exhibit a unique ordering throughout the table. The results therefore support the voltage trend but do not justify a general statement that one face-sheet porosity pattern always gives the highest frequency.

Table 7. Effect of applied voltage on the dimensionless frequency.

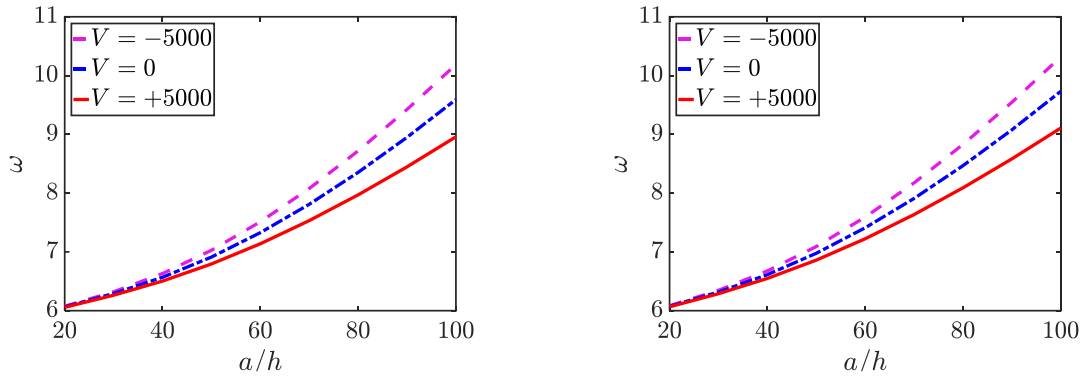
Face layer	V (V)	SSSS	CCCC	SCSC	SCSF
FGPie-0	-1200	9.6885	20.1470	15.7509	6.8085
	0	9.5081	20.0405	15.6273	6.6204
	+1200	9.3242	19.9334	15.5026	6.4256
FGPie-I	-1200	9.6425	20.1222	15.7204	6.7714
	0	9.4924	20.0338	15.6178	6.6148
	+1200	9.3399	19.9450	15.5145	6.4535
FGPie-II	-1200	9.6841	20.1461	15.7488	6.8047
	0	9.5074	20.0418	15.6278	6.6205
	+1200	9.3274	19.9369	15.5058	6.4298

The effect of the geometric ratio b/a is shown in Fig. 6. With a fixed and b increased, the dimensionless frequency decreases for all four boundary conditions and for both core-porosity distributions. The reduction is strongest at small b/a, after which the response gradually levels off as the plate becomes longer in the y direction. The boundary-condition ordering remains CCCC > SCSC > SSSS > SCSF.



(a) SPD (b) ASPD

Figure 6. Effect of b/a on the dimensionless frequency: (a) SPD; (b) ASPD.



(a) SPD (b) ASPD

Figure 7. Effect of a/h and applied voltage on the dimensionless frequency: (a) SPD; (b) ASPD.

Figure 7 examines the combined effects of the slenderness ratio a/h and applied voltage for the SSSS plate. For this figure, the layer-thickness configuration is 1-4-1, while the stiffener width and height are fixed at 0.015 m and 0.020 m, respectively. Under the present definition of the dimensionless frequency, $\overline{\omega}$ increases as a/h increases. This is a trend of the normalized quantity and should not be interpreted directly as an increase in the dimensional frequency in hertz as the plate becomes thinner. At every a/h, the $V = -5000\ V$ curve lies highest and the $V = +5000\ V$ curve lowest; the separation between the curves increases for thinner plates. This is consistent with the electrically induced geometric-stiffness contribution becoming more significant relative to bending stiffness as a/h increases.

3.2.4. Effect of thermal field

Thermal effects are examined over $0 \leq \Delta T \leq 60\ K$ so that all cases in Fig. 8 remain on the stable fundamental branch with a positive fundamental eigenvalue $\lambda > 0$. Over this range, the frequency decreases monotonically with increasing temperature for all four boundary conditions and for UTR, LTR, and NLTR. UTR gives the largest reduction because the full thickness experiences the same temperature rise and therefore develops a larger compressive thermal membrane force. LTR and NLTR have lower through-thickness average temperature rises and correspondingly smaller frequency reductions.

At $\Delta T = 60\ K$, the SSSS frequency decreases from 10.9215 to 7.4118, 9.3311, and 9.7564 for UTR, LTR, and NLTR, corresponding to reductions of about 32.1%, 14.6%, and 10.7%,

respectively. The thermal effect is especially pronounced for SCSF: at 60 K, UTR reduces the frequency by about 66.3%, whereas LTR and NLTR reduce it by about 24.2% and 17.2%. The study is limited to 60 K to avoid the range in which the fundamental eigenvalue approaches instability and to remain consistent with the assumption of temperature-independent material coefficients. Determining the critical temperature is outside the scope of the present work.

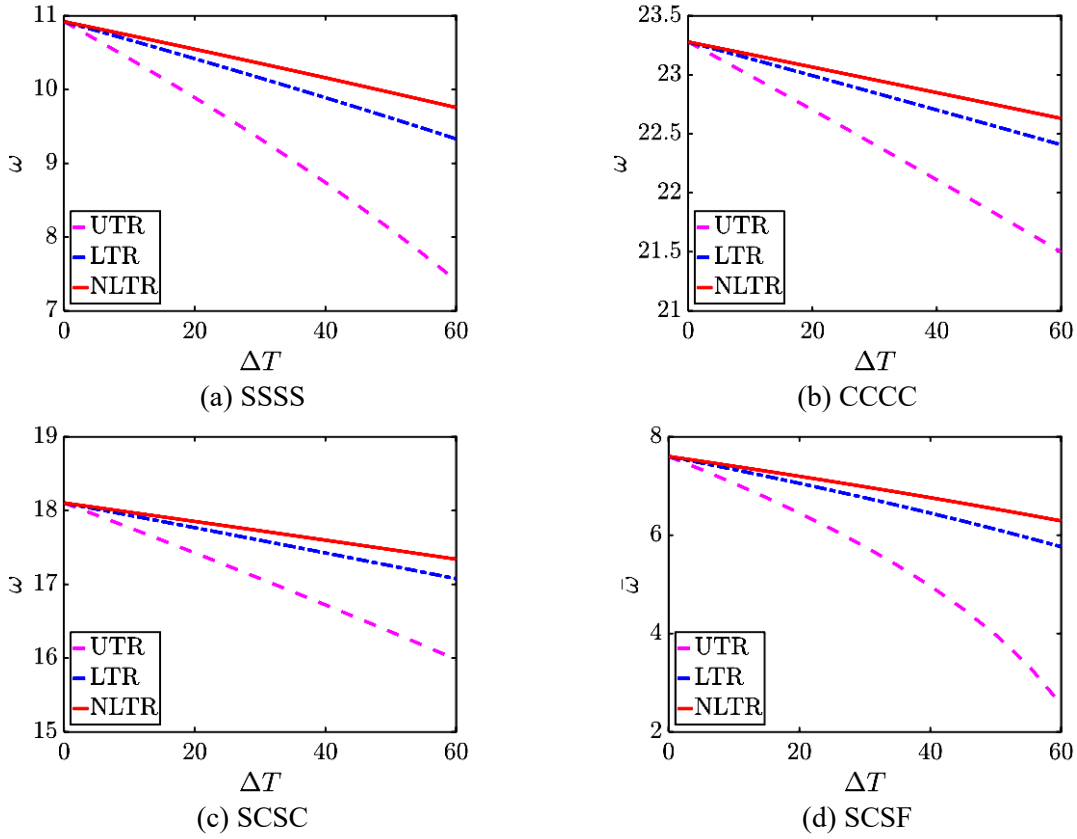


Figure 8. Effect of temperature rise ΔT on $\overline{\omega}$: (a) SSSS; (b) CCCC; (c) SCSC; (d) SCSF.

4. CONCLUSION

A semi-analytical HSDT4/pb²-Ritz model is developed for the electro-thermoelastic free vibration of SFGP-Pie sandwich plates with a porous metal-foam core and orthogonal FGM stiffeners. The formulation includes a cosine-linear electric potential and thermal/electrical prestress. The main findings are summarized as follows:

- The model converges stably; the maximum differences are 1.993% against the stiffened-plate FEM benchmark [30] and 0.018% against the coupled MEE-FG benchmark [8].

- Within the investigated range, increasing core porosity raises the dimensionless frequency because mass reduction dominates stiffness loss, with ASPD slightly above SPD. The p_z index is much more influential than p_{Pie}, while core-thickness effects are small and not universally monotonic.

- Increasing stiffener number and h_s/b_s generally raise the frequency, but the gain depends on boundary condition and orientation; for SCSF, two-directional stiffening is not always the most effective arrangement.

- Negative voltage stiffens the plate and positive voltage softens it. FGPie-0, FGPie-I, and FGPie-II show no universal ordering. Increasing b/a lowers the dimensionless frequency, whereas increasing a/h raises the normalized quantity without implying a higher dimensional frequency.

- Thermal loading lowers the frequency; UTR gives the largest decrease, followed by LTR and NLTR, with SCSF the most temperature-sensitive. The range $\Delta T \leq 60\ K$ keeps all reported cases on the positive fundamental-eigenvalue branch.

The results offer preliminary design guidance within the studied ranges: stiffener number, height, and orientation should be selected together with the boundary condition, while UTR is the most adverse thermal case. The model addresses global response under perfect bonding; local stiffener effects, interface degradation, alternative potential functions, and temperature-dependent properties remain for future work.

ACKNOWLEDGMENT

This research is funded by Ministry of Education and Training under grant number B2025-XDA-06.

REFERENCES

[1]. B. Behjat, M. Salehi, M. Sadighi, A. Armin, M. Abbasi, Static, dynamic, and free vibration analysis of functionally graded piezoelectric panels using finite element method, Journal of Intelligent Material Systems and Structures, 20 (2009) 1635-1646. https://doi.org/10.1177/1045389X09104113

[2]. X.-H. Wu, C. Chen, Y.-P. Shen, X.-G. Tian, A high order theory for functionally graded piezoelectric shells, International Journal of Solids and Structures, 39 (2002) 5325-5344. https://doi.org/10.1016/S0020-7683(02)00418-3

[3]. M.R. Sedighi, M. Shakeri, A three-dimensional elasticity solution of functionally graded piezoelectric cylindrical panels, Smart Materials and Structures, 18 (2009) 055015. https://doi.org/10.1088/0964-1726/18/5/055015

[4]. Y.Q. Wang, Electro-mechanical vibration analysis of functionally graded piezoelectric porous plates in the translation state, Acta Astronautica, 143 (2018) 263-271. https://doi.org/10.1016/j.actaastro.2017.12.004

[5]. Z. Zhong, T. Yu, Vibration of a simply supported functionally graded piezoelectric rectangular plate, Smart Materials and Structures, 15 (2006) 1404-1412. https://doi.org/10.1088/0964-1726/15/5/029

[6]. M.R. Barati, A.M. Zenkour, Electro-thermoelastic vibration of plates made of porous functionally graded piezoelectric materials under various boundary conditions, Journal of Vibration and Control, 24 (2018) 1910-1926. https://doi.org/10.1177/1077546316672788

[7]. I. Esen, K.G. Aktaş, F. Pehlivan, Investigation of the critical buckling temperatures and free vibration response of porous functionally graded magneto-electro-elastic sandwich higher-order nanoplates with temperature-dependent material properties, Journal of Vibration Engineering & Technologies, 13 (2025) 162. https://doi.org/10.1007/s42417-024-01542-6

[8]. F. Ebrahimi, A. Jafari, M.R. Barati, Vibration analysis of magneto-electro-elastic heterogeneous porous material plates resting on elastic foundations, Thin-Walled Structures, 119 (2017) 33-46. https://doi.org/10.1016/j.tws.2017.04.002

[9]. M. Askari, A.R. Saidi, A.S. Rezaei, On natural frequencies of Levy-type thick porous-cellular plates surrounded by piezoelectric layers, Composite Structures, 179 (2017) 340-354. https://doi.org/10.1016/j.compstruct.2017.07.073

[10]. M. Askari, A.R. Saidi, A.S. Rezaei, An investigation over the effect of piezoelectricity and porosity

distribution on natural frequencies of porous smart plates, Journal of Sandwich Structures & Materials, 22 (2020) 2091-2124. https://doi.org/10.1177/1099636218791092

[11]. H.-Q. Tran, V.-T. Vu, M.-T. Tran, Free vibration analysis of piezoelectric functionally graded porous plates with graphene platelets reinforcement by pb-2 Ritz method, Composite Structures, 305 (2023) 116535. https://doi.org/10.1016/j.compstruct.2022.116535

[12]. D.O. Brush, B.O. Almroth, Buckling of Bars, Plates, and Shells, McGraw-Hill, New York, 1975.

[13]. M.M. Najafizadeh, A. Hasani, P. Khazaeinejad, Mechanical stability of functionally graded stiffened cylindrical shells, Applied Mathematical Modelling, 33 (2009) 1151-1157. https://doi.org/10.1016/j.apm.2008.01.009

[14]. D.D. Thuy, B.D. Huy, N.P. Nhu, H.P. Thanh, P.N. Thi, Nonlinear buckling and postbuckling analysis of FG-GRMMC cylindrical panels with oblique and orthogonal stiffeners in thermal environment, Transport and Communications Science Journal, 77 (2026) 70-84. https://doi.org/10.47869/tcsj.77.1.6

[15]. P.H. Cong, P.K. Quyet, N.D. Duc, Effects of lattice stiffeners and blast load on nonlinear dynamic response and vibration of auxetic honeycomb plates, Proceedings of the Institution of Mechanical Engineers, Part C: Journal of Mechanical Engineering Science, 235 (2021) 7192-7211. https://doi.org/10.1177/0954406221992797

[16]. H.-A. Pham, H.-Q. Tran, M.-T. Tran, V.-L. Nguyen, Q.-T. Huong, Free vibration analysis and optimization of doubly-curved stiffened sandwich shells with functionally graded skins and auxetic honeycomb core layer, Thin-Walled Structures, 179 (2022) 109571. https://doi.org/10.1016/j.tws.2022.109571

[17]. D. Van Dung, N.T. Nga, Thermomechanical postbuckling analysis of eccentrically stiffened FGM sandwich plates with general Sigmoid and power laws based on TSDT, Journal of Sandwich Structures & Materials, 20 (2018) 907-945. https://doi.org/10.1177/1099636216682545

[18]. T.-T. Pham, H.-Q. Tran, V.-L. Nguyen, K.-H. Le, M.-T. Tran, Free and forced vibration of functionally graded porous sandwich plates reinforced by arbitrarily oblique stiffeners, Thin-Walled Structures, 210 (2025) 113039. https://doi.org/10.1016/j.tws.2025.113039

[19]. T.-T. Pham, H.-Q. Tran, M.-T. Tran, H.-N. Nguyen, V.-T. Vu, Vibration behavior of stiffened functionally graded porous sandwich plates with a magneto-electro-elastic face resting on an elastic foundation under hygrothermal, electrical, and magnetic fields, Mechanics Based Design of Structures and Machines, 54 (2026) 2574890. https://doi.org/10.1080/15397734.2025.2574890

[20]. V.-T. Vu, H.-Q. Tran, Free vibration characteristics of stiffened sandwich plates with auxetic core and functionally graded piezoelectric face sheet, Acta Mechanica, 235 (2024) 4029-4056. https://doi.org/10.1007/s00707-024-03932-z

[21]. N. Wattanasakulpong, V. Ungbhakorn, Linear and nonlinear vibration analysis of elastically restrained ends FGM beams with porosities, Aerospace Science and Technology, 32 (2014) 111-120. https://doi.org/10.1016/j.ast.2013.12.002

[22]. C. Liang, Y.Q. Wang, A quasi-3D trigonometric shear deformation theory for wave propagation analysis of FGM sandwich plates with porosities resting on viscoelastic foundation, Composite Structures, 247 (2020) 112478. https://doi.org/10.1016/j.compstruct.2020.112478

[23]. M. Bodaghi, M. Shakeri, An analytical approach for free vibration and transient response of functionally graded piezoelectric cylindrical panels subjected to impulsive loads, Composite Structures, 94 (2012) 1721-1735. https://doi.org/10.1016/j.compstruct.2012.01.009

[24]. G. Shi, A new simple third-order shear deformation theory of plates, International Journal of Solids and Structures, 44 (2007) 4399-4417. https://doi.org/10.1016/j.ijsolstr.2006.11.031

[25]. H.Q. Tran, V.-T. Vu, M.T. Tran, P. Nguyen-Tri, A new four-variable refined plate theory for static analysis of smart laminated functionally graded carbon nanotube reinforced composite plates, Mechanics of Materials, 142 (2020) 103294. https://doi.org/10.1016/j.mechmat.2019.103294

[26]. H.-Q. Tran, V.-C. Nguyen, T.-P. Hoang, Vibration and buckling of sandwich plates with honeycomb auxetic core and three-phase bi-directional functionally graded face sheets, Engineering Structures, 343 (2025) 121133. https://doi.org/10.1016/j.engstruct.2025.121133

[27]. Q. Wang, Axi-symmetric wave propagation in a cylinder coated with a piezoelectric layer, International Journal of Solids and Structures, 39 (2002) 3023-3037. https://doi.org/10.1016/S0020-7683(02)00233-0

[28]. L. Wu, Y. Lu, Free vibration analysis of rectangular plates with internal columns and uniform elastic edge supports by pb-2 Ritz method, International Journal of Mechanical Sciences, 53 (2011) 494-504. https://doi.org/10.1016/j.ijmecsci.2011.04.006

[29]. Q. Li, V.P. Iu, K.P. Kou, Three-dimensional vibration analysis of functionally graded material sandwich plates, Journal of Sound and Vibration, 311 (2008) 498-515. https://doi.org/10.1016/j.jsv.2007.09.018

[30]. I.E. Harik, M. Guo, Finite element analysis of eccentrically stiffened plates in free vibration, Computers & Structures, 49 (1993) 1007-1015. https://doi.org/10.1016/0045-7949(93)90012-3